applied sciences

MDPI

Article

Experimental and Numerical Analysis of the Progressive Damage and Failure of SiC_f/TC_4 Composite Shafts

Li Luo [1], Jingxuan Wang [1], Yundong Sha [1,*], Yanping Hao [2] and Fengtong Zhao [1]

[1] Key Laboratory of Advanced Measurement and Test Technique for Aviation Propulsion System, Shenyang Aerospace University, Shenyang 110136, China; luolisau@163.com (L.L.); jingxuanwang419@163.com (J.W.); zhao_ft@buaa.edu.cn (F.Z.)

[2] AECC Shenyang Engine Research Institute, Shenyang 110015, China; shluoli@126.com

* Correspondence: ydsha2003@vip.sina.com

Abstract: Long fibre-reinforced metal matrix composite materials, which are widely used in industry, have complex and diverse damage modes due to their structural characteristics. In this study, the progressive damage process and failure mode analysis of the SiC_f/TC_4 composite shafts were thoroughly investigated under single torsional loads. A bearing performance test was carried out, the damage process was monitored using acoustic emissions, and the fracture specimens were analysed using a scanning electron microscope (SME). More specifically, under reverse torque loading, the damage process was slow-varying, the interface was subjected to tensile force, and fracture occurred mostly in the form of interface cracking; further, the breaking load of the specimen was 11,812 Nm. Under forward loading, the damage process was fast-varying. The fibres were subjected to tensile forces, and the fracture form was mostly fibre fracture; the breaking load of the specimen was 10,418 Nm. Under torque loading, the first damage to the specimens appeared in the outermost layer of the composite material's reinforced section, and the initial cracking position was at the interface, expanding from the outside to the inside. Based on the principles of macro-mechanics and micro-mechanics theory, the cross-scale models were proposed, which contain the shaft with the same dimensions as the specimen and a micro-mechanics representative volume element (RVE) model. The initial interface damage load was 6552 Nm under reverse torque loading. Under forward loading, the initial interface damage load was 9108 Nm. In comparison to the acoustic emission test results, the main goal was to calculate the progressive damage process under the same conditions as the experiment, verifying the effectiveness of the cross-scale models.

Keywords: SiC_f/TC_4 composite shaft; progressive damage; failure modes; cross-scale models; experiment

Citation: Luo, L.; Wang, J.; Sha, Y.; Hao, Y.; Zhao, F. Experimental and Numerical Analysis of the Progressive Damage and Failure of SiC_f/TC_4 Composite Shafts. *Appl. Sci.* **2023**, *13*, 6232. https://doi.org/10.3390/app13106232

Academic Editor: Theodore E. Matikas

Received: 10 April 2023
Revised: 4 May 2023
Accepted: 8 May 2023
Published: 19 May 2023

1. Introduction

It is well-established that weight reduction and increases in efficiency are the design requirements of next-generation aero-engines. Without changing the structural layout, new types of materials with unique properties should be fabricated [1–3]. From this perspective, metal matrix composites have a higher specific strength and specific stiffness than conventional metallic materials [4,5]. The SiC_f/TC_4 composite is a type of long fibre-reinforced metal matrix composite that has been widely used in the shafts of many engines to achieve the above-mentioned objectives [6,7]. The damage processes of SiC_f/TC_4 composites, which are regarded to be anisotropic materials, are complex and diverse. Further, the shaft also needs to withstand torque as it is a relatively important transmission component [8]. Therefore, a deep understanding of the damage evolution and failure modes of composite shafts can provide guidance for their application in aero-engines.

Shafts are core components in all mechanical equipment because they support rotating devices and transmit motion, torque, or bending moment. A large number of experimental studies and simulation calculations have been performed on the damage mechanism, failure mode, and fatigue fracture of these components [9,10]. GE and Pratt & Whitney [11] successfully applied a SiC_f/TC_4 composite turbofan shaft to an XTE-45 engine, with a total length of 127 cm and a layup of $[\pm 15°]_{36}$. GE Aero Engines developed four specimens of fibre-reinforced titanium matrix composite cylindrical shafts. They conducted vibration modal analysis and failure mode analysis experiments under normal- and high-temperature conditions [12,13]. Further, Trifkovic analysed the failure causes of a combat jet aircraft rudder shaft (RS) during flight missions using a finite element method, proposing new design suggestions [14]. In 2005, the University of Nottingham and the European Commission jointly conducted the VITAL project to develop a total of 24 specimens with SiC_f/Ti-6Al-4V composite shafts. Moreover, stiffness tests, fatigue tests, and failure mode analyses were carried out, as well as numerical calculations and model validation [15,16]. All studies on shaft damage, failure, and fatigue aimed to better transfer the load to mechanical equipment and yield a more optimal design of the shaft [17,18].

At present, there are various methods for progressive damage analysis, most of which focus on numerical calculations and experimental studies [19,20]. Usually, a numerical model is established, and an appropriate failure criterion is selected according to the computation module [21]. For example, Riccio [22] studied the shear behaviour of a stiffened composite panel with a notch through numerical simulation using a three-dimensional progressive degradation model, establishing a new method to take into account the gradual intra-laminar degradation of composite laminates. Zhang et al. [23] also used a single-cell model with fibre hexagonal distribution to predict the fibre's bundle properties and then simulated the progressive damage process of triaxial woven composites. In another study, Himayat [24] established a new method to model the interactions between interface debonding and skin damage, based on the cohesive zone model and continuum damage mechanics scheme; this method can facilitate progressive damage analysis of a blade under extreme loading. Han used a novel method to evaluate fatigue damage under sub-synchronous oscillation incidents, which utilizes field data, modal decomposition, and superposition, combining structural full-size finite-element modal analysis with the refined finite-element structural analysis of specific parts [25]. Jeng et al. [26] provided a continuous SiC fibre-reinforced Ti-25-10 titanium alloy composite with tensile damage fracture characteristics, along with the damage mechanism at the strong and weak interfaces and the surface characteristics of the tensile fracture. A significant amount of research based on the analysis method of cross-scale mechanics has also been conducted [27,28].

Most research in this field has focused on the failure mode of metal drive shafts and composite plates or shells. However, the damage process and the failure modes of composite shafts have not been studied sufficiently, especially in terms of the microscopic failure modes and failure processes, such as fibre fracture, matrix damage, and interface cracking. Therefore, it is imperative to conduct damage process analysis and failure mode research on SiC_f/Ti composite shafts.

Therefore, in this study, torsional strength experiments and failure mode analyses on SiC_f/TC_4 composite shafts were carried out. The damage process trend of the shaft was monitored using acoustic emissions, and the onset of shaft fracture was examined by carrying out electron microscopy experiments. A macro-mechanics shaft model and a micro-mechanics RVE model were also established. Based on the two models, the damage processes of fibre fracture, matrix cracking, and interface debonding under torque loads were calculated by the finite-element method. The main goal was to calculate the progressive damage process under the same conditions as the experiment, verifying the effectiveness of the cross-scale models. This can provide design support for shaft applications in aero-engines.

2. Theoretical Modelling

2.1. Periodic Boundary Conditions

The SiC_f/TC_4 composite shaft has a cylindrical structure and is synthesized by the lamination of multiple layers of fibre-reinforced composites. Fibre-reinforced metal matrix composite shafts are prepared through a fibre-winding process [1,28,29], and can be divided into single-cell RVEs, periodically arranged RVEs, single-layer materials, and laminated materials. Further, the order of material structure scales—from small to large—is from macro-mechanical to micro-mechanical [7], as shown in Figure 1.

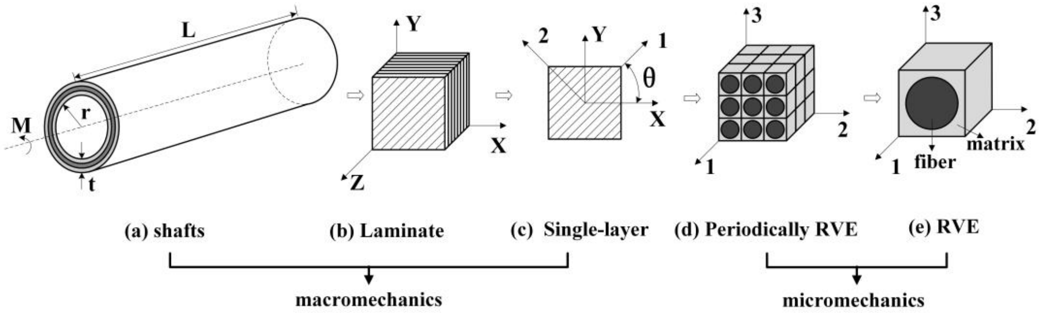

Figure 1. Macro–micro mechanical scales of the fibre-reinforced metal matrix composite shaft. (Principal coordinate system-XYZ and Off-axis coordinate system-123).

As shown in Figure 2, the simplified geometric model of the RVE is a cube with side length L, where A_i (i = 1, 2, ... 8) denotes the vertices of the RVE and B_i (i = 1, 2, ... 12) refers to the edges of the RVE. The boundary surfaces of the RVE are represented by C_{ij}.

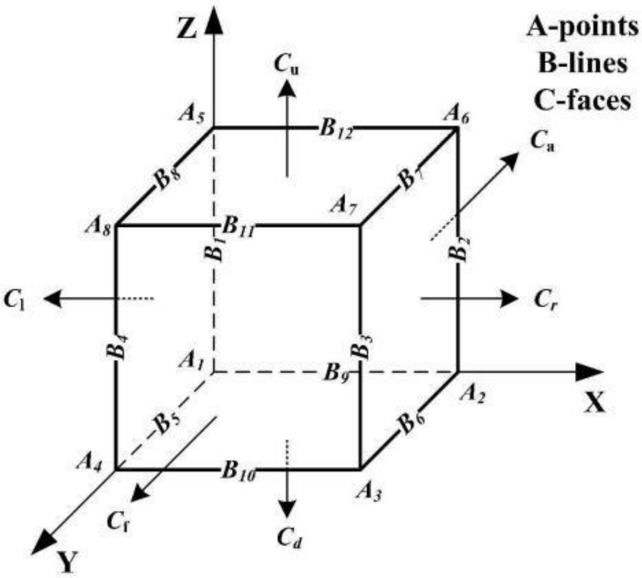

Figure 2. Simplified description of the RVE.

When the RVE is initially undeformed, M_{Q1} and M_{Q2} are the position vectors of any points Q_1 and Q_2 on the initial model surface C_l and C_r, respectively. M_{A1} and M_{A2} represent the initial vectors of the vertex A_1 and A_2 of the model, and T_{Q1} andT_{Q2} denote the shape vector of points Q_1 and Q_2 on the initial model surface C_l and C_r for the RVE, respectively, expressed as follows:

$$T_{Q1} = M_{Q1} - M_{A1} \tag{1}$$

$$T_{Q2} = M_{Q2} - M_{A2} \tag{2}$$

When the RVE is deformed, N_{Q1} and N_{Q2} denote the vectors of any points Q_1 and Q_2 on the initial model surface C_l and C_r, respectively. N_{A1} and N_{A2} denote the initial vectors of the vertices A_1 and A_2 of the model, respectively, and P_{Q1} and P_{Q2} refer to shape vectors of points Q_1 and Q_2 on the initial model surfaces C_l and C_r for the RVE, respectively, which can be expressed as follows:

$$P_{Q1} = N_{Q1} - N_{A1} \tag{3}$$

$$P_{Q2} = N_{Q2} - N_{A2} \tag{4}$$

According to the RVE displacement continuity condition, the variables of the model corresponding to the boundary always remain the same, namely T_{Q1} equals P_{Q1} and T_{Q2} equals P_{Q2}. When the RVE is deformed, R_{Q1} and R_{Q2} represent the displacement vectors of any points Q_1 and Q_2 on the initial model surface C_l and C_r, respectively, and R_{A1} and R_{A2} denote the displacement vectors of the vertices A_1 and A_2. Thus,

$$N_{Q1} = M_{Q1} + R_{Q1} \tag{5}$$

$$N_{Q2} = M_{Q2} + R_{Q2} \tag{6}$$

$$N_{A1} = M_{A1} + R_{A1} \tag{7}$$

$$N_{A2} = M_{A2} + R_{A2} \tag{8}$$

In summary, the displacement vectors can be expressed as follows:

$$R_{Q2} = R_{Q1} + (R_{A2} - R_{A1}) \tag{9}$$

Similarly, other faces can also be formulated. Hence, it can be argued that all the node displacements in the symmetry plane during the deformation of RVE can be accurately determined by the corresponding nodes in their symmetry plane.

The RVE satisfies the stress values of equal magnitude and opposite direction on its opposing surfaces to fully ensure that the stress field is continuous and uninterrupted between neighbouring RVEs. More specifically, when the RVE is deformed, its Y-direction is known by the RVE element stress continuity condition, while the stress components on the external surface of the RVE element deformation can be expressed using the following equations:

$$\sigma_+ - \sigma_- = 0 \tag{10}$$

$$\tau_+ - \tau_- = 0 \tag{11}$$

where σ is the normal force on the corresponding surface in the Y-direction,τ denotes the tangential force on the corresponding surface in the Y-direction, and + and − represent any two boundary parallel surfaces in the Y-direction.

$$\mathrm{s}_y = \bar{\varepsilon}_y y + s_y^* \tag{12}$$

where $\bar{\varepsilon}_v$ is the average strain of the RVE with periodicity, $\bar{\varepsilon}_v y$ stands for the linearly distributed displacement field to reflect the periodic uniformity of the RVE, and s_v^* denotes the displacement correction of the RVE, which is determined by the internal composition structure of the composite. For the long fibre-reinforced structure, this variable has a global periodic character. If a cell contains any of the RVEs in the structure, it should comply with the following boundary condition:

$$s_v^+ - s_v^- = \bar{\varepsilon}_v \Delta y \tag{13}$$

In addition, if the RVE has been defined to be periodic, Δy should be a constant, and $\bar{\varepsilon}_v$ represents the overall average strain component of the composites, which is constant in a structure with uniformly arranged reinforcements in the same material. Therefore,

$\bar{\varepsilon}_v \Delta y$ is a constant. If the corresponding boundary displacements S_a and S_b for the RVE simultaneously satisfy Equation (13), then we obtain the following equation:

$$\Delta S = S_a - S_b \tag{14}$$

Following the minimum strain energy principle, if the minimum strain energy reaches a minimum value, then $\Delta S = 0$, at which point there is only one solution when the displacement boundary condition is imposed on the RVE.

The planar structure of the RVE of a single fibre-reinforced composite is shown in Figure 3.

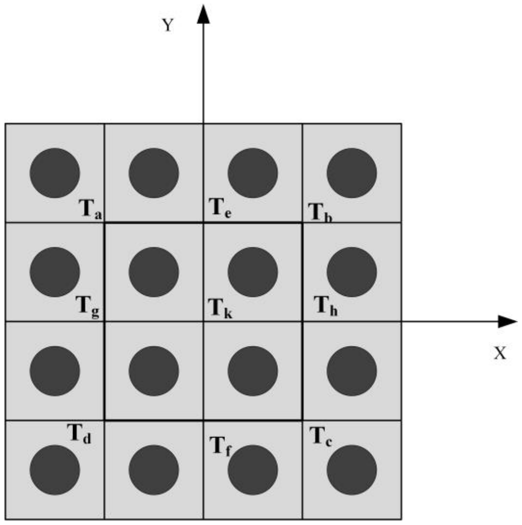

Figure 3. The 2-D periodic structure of the RVEs.

Displacement continuity boundary conditions are imposed on cells $T_aT_bT_cT_d$, $T_aT_eT_kT_g$, $T_eT_bT_hT_k$, etc., if it is assumed that these RVEs cannot satisfy the stress continuity. Then, for the element $T_aT_bT_cT_d$, the following equation will apply:

$$\sigma_{ag} \neq \sigma_{bh} \tag{15}$$

where σ_{ij} is the RVE corresponding to the normal force outside the boundary.

Additionally, for the other RVE $T_aT_eT_kT_g$, the following expression holds:

$$\sigma'_{bh} \neq \sigma_{ek} \tag{16}$$

where σ'_{ij} denotes the RVE corresponding to the force normal to the right side of the boundary.

From Equations (15) and (16), it can be found that

$$\sigma'_{bh} \neq \sigma_{bh} \tag{17}$$

It is important to note that Equation (17) is obviously not consistent with the practical situation. In particular, if the previous assumptions do not hold, the RVE can ensure that the normal stress continuity condition is satisfied. Similarly, the shear stress continuity condition can be also proven to hold simultaneously using this method. In summary, the corresponding stress continuity boundary condition is automatically satisfied when the displacement continuity boundary condition is applied to the RVE with a periodic arrangement.

2.2. Derivation of the Damage Evolution States

According to the conclusions drawn in a study by Echaabi [29], the Hashin criterion is able to distinguish the physical properties of fibre and matrix damage. Therefore, the Hashin criterion was used to determine the damage initiation during the progressive failure analysis herein; the progressive failure flow, combined with the computational model in this paper, is illustrated in Figure 4. The following five different damage modes were considered in the model: fibre tensile failure, fibre compression failure, matrix tensile failure, matrix compression failure, and matrix fibre shear failure [30,31]. As far as the fibre-reinforced metal matrix composite is concerned, the stress–strain relationship in the principal coordinate system can be expressed as follows:

$$\begin{Bmatrix} \sigma_{11} \\ \sigma_{22} \\ \tau_{12} \end{Bmatrix} = \begin{bmatrix} E_1 & \gamma_{21}E_1 & 0 \\ \gamma_{12}E_2 & E_2 & 0 \\ 0 & 0 & G_{12} \end{bmatrix} \tag{18}$$

where E_1 and E_2 are the longitudinal and transverse moduli of elasticity, respectively; γ_{21} and γ_{12} denote Poisson's ratios; and G_{12} is the shear modulus. According to the classical laminate theory, the following expression can be derived:

$$\sigma' = C_0\varepsilon \tag{19}$$

where C_0 is the composite stiffness matrix and the principal coordinate system of the fibre-reinforced composite monolayer structure shown in Figure 1.

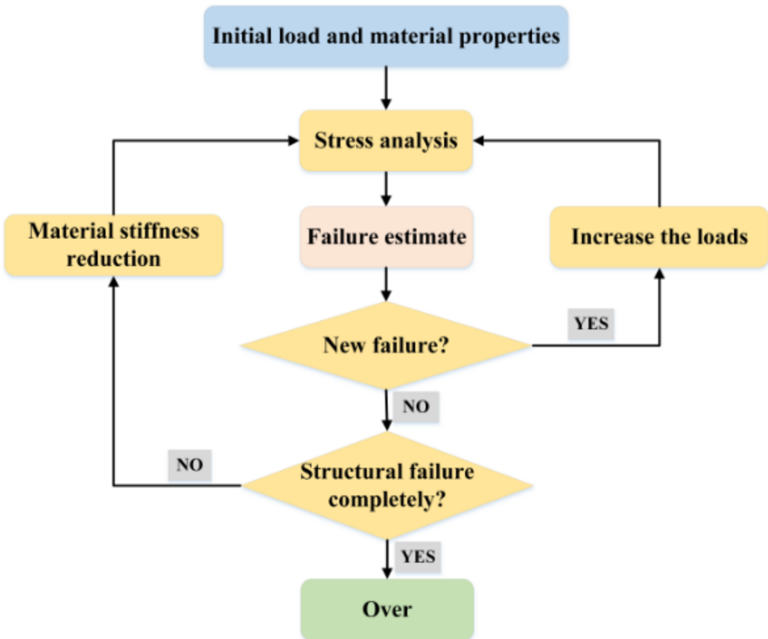

Figure 4. Progressive failure calculation flow.

When local damage is generated in the material, the stiffness degradation due to the damage is considered. Based on the principle of material property degradation (MPDG), the constitutive equation of the material is defined as follows:

$$\sigma = C_d\varepsilon \tag{20}$$

where C_d denotes the damage stiffness matrix. The damage stiffness matrix of the transversely isotropic material C_d for the plane stress state can be expressed as follows:

$$C_d = (1-d_i)C_0 = \frac{1}{D}\begin{bmatrix} (1-d_f)E_1 & (1-d_f)(1-d_m)\gamma_{12}E_1 & 0 \\ (1-d_f)(1-d_m)\gamma_{12}E_2 & (1-d_m)E_2 & 0 \\ 0 & 0 & (1-d_s)G_{12}D \end{bmatrix} \tag{21}$$

where $D = 1-(1-d_f)(1-d_m)\gamma_{12}\gamma_{21}$, d_f, d_m, and d_s are the fibre, matrix, and shear damage state variables, respectively. The damage state variables have values between 0 and 1. When the damage state variable is 0, it means that the element has experienced no damage and that the material stiffness has not changed. On the other hand, when the damage state variable is 1, it implies that the element has completely failed and that the material stiffness is 0.

Where the superscript *t* indicates stretching and specifies *c* compression for *d*. After the damage has occurred, the effective stress of the material is $\hat{\sigma} = M\sigma$, where the damage matrix *M* is defined as follows:

$$M = \begin{bmatrix} \frac{1}{1-d_f} & 0 & 0 \\ 0 & \frac{1}{1-d_m} & 0 \\ 0 & 0 & \frac{1}{1-d_s} \end{bmatrix} \tag{22}$$

The local damage within the composite degrades the material properties, the stiffness of the damaged element is lowered, and the stress values are redistributed [31]. The stress increase near the damage site is also larger, and failure is more likely to occur when the load increases, causing the gradual expansion of damage. Figure 5 depicts the damage evolution pattern of the linear elastic material.

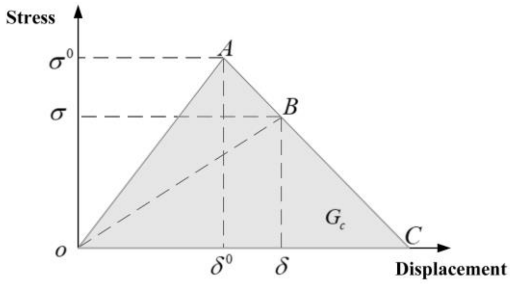

Figure 5. Diagram of the damage evolution pattern of the linear elastic material.

In Figure 5, section OA indicates the state of the composite material without damage, whereas section AC shows the degradation of the material after the damage has occurred. During the process of stiffness reduction of the material, the damage factor *d* is defined as follows:

$$d = \frac{\delta^f(\delta - \delta^0)}{\delta(\delta^f - \delta^0)} \tag{23}$$

The damage initiation displacement can be calculated by the following expression: $\delta^0 = L_C \varepsilon^0$, where the damage initiation strain is defined as follows: $\varepsilon^0 = X/E$. The complete failure displacement can be expressed as follows: $\delta^f = 2G_c/\sigma^0$, where G_c is the fracture toughness (this is the shaded area in Figure 5).

After the degradation of the stiffness of the material's damaged part, a new stiffness matrix C_d can be obtained, which is rebalanced under the original load. As the external load increases, the damage accumulates and superimposes until final failure.

3. Experiment

3.1. Experimental Materials

The experiment was conducted using the SiC_f/TC_4 composite shaft; the SiC fibres were manufactured at the Institute of Metal Research, Chinese Academy of Sciences. Significant research has been conducted on RF fibre production, as well as on the use of the DC method for SiC fibre deposition and its growth principle. Further, gas reduction cleaning technology has been proposed by the Institute of Metal Research. In this technique, H_2—with a large specific heat capacity and strong reduction potential—is introduced into the reaction vessel. This H_2, which acts on the surfaces of the W filament, is cleaned and cooled. In the deposition stage of SiC, the reaction gas is introduced to control the ratio of the reaction gas, flow and velocity, and deposition temperature. Finally, the concentration field and temperature distribution suitable for the stable growth of deposited SiC is obtained, which ensures the fine grain organization of SiC fibres. This is a comprehensive and integrated short process that facilitates W filament cleaning, SiC deposition, and coating deposition in the same reaction vessel through the design of the reaction vessel's shape and structure, especially the control of the gas flow path. This must be coordinated with the comprehensive correlation regulation of the reaction gas type, concentration, flow rate, deposition temperature, and wire resorbing speed.

The SiC layer was deposited on a tungsten monofilament by chemical vapour deposition. A carbon coating with a thickness of 2 μm was also produced to prevent a reaction between the SiC layer and titanium alloy. The total diameter of the SiC fibre was about 100 μm, and the average tensile strength was about 3600 MPa, with a high modulus that was subjected to Weibull analysis [32]. The Ti matrix composites were fabricated via the matrix-coated fibre route to achieve a homogeneous distribution. The matrix, with a nominal composition of Ti–6Al–4V, was deposited on SiC fibres using magnetron sputtering [33]. The coated fibres were wound at 45° orientations and finally consolidated into matrix claddings through hot isostatic pressing. It has a total of two types of plies, 6-ply and 10-ply. All parts other than the test section were Ti, and the $[45°]_6$ specimen drawing is shown in Figure 6. The images of the two specimens are shown in Figure 7a; the cross-section morphology of the other test pieces were observed after dissection, as shown in Figure 7b,c.

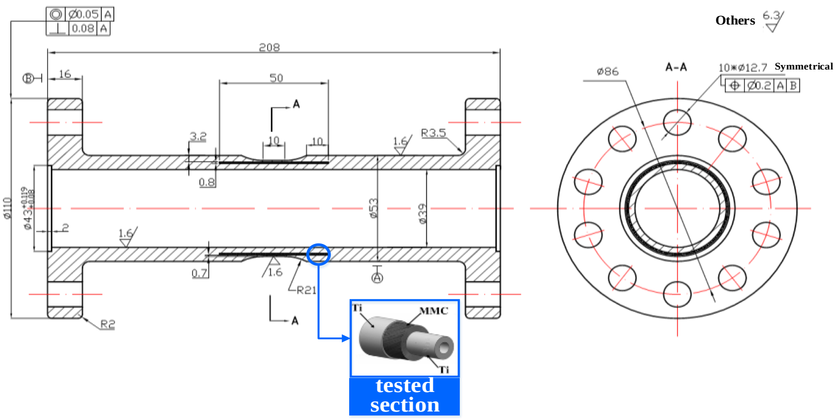

Figure 6. Dimensional structure of the specimen.

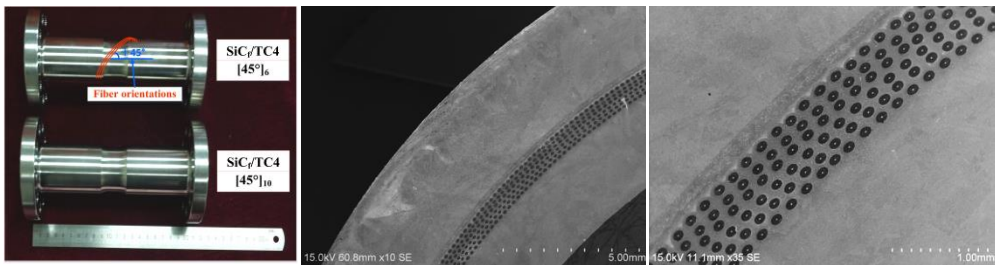

(**a**) (**b**) (**c**)

Figure 7. Photograph of the specimens and the cross-section morphology: (**a**) the specimens; (**b**) the entire cross-section morphology; and (**c**) the partial cross-section morphology.

All experiments were conducted at room temperature, and the servo cylinder was controlled by the hydraulic drive system. One section of the swing arm was connected to the cylinder, and the other end was connected to the specimen adapter section. Further, one section of the specimen was fixed to the adapter section, and the torque was applied to the adapter section by the swing arm and then transferred to the specimen. The other end of the specimen was fixed by full restraint; the installation of the experimental system devices and the specimen are shown in Figure 8a,b. The entire experimental process was controlled by the computer, which was connected to an MTS Flextest200 controller (Germany), and the controller was connected to the torque sensor and the hydraulic servo valve through the cable. The servo valve controls the oil in and out of the hydraulic cylinder according to the command value given by the computer, as shown in Figure 8c.

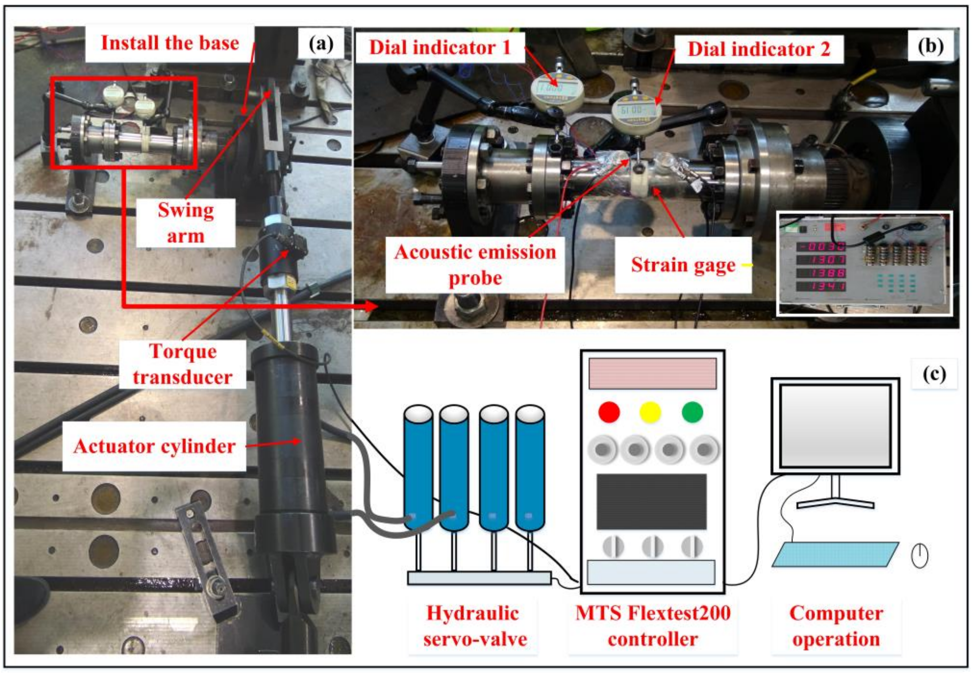

Figure 8. Test system layout: (**a**) test system device; (**b**) measuring equipment; and (**c**) operating end and controller.

Damage detection was performed through both destructive and non-destructive testing using a Hitachi S-3400N (Japan) scanning electron microscope to observe the longitudinal profile morphology near the sample fracture. A PCI-2 acoustic emission system from Physical Acoustics was used to monitor the damage evolution non-destructively. Two broadband (200–900 kHz) acoustic emission sensors were also mounted symmetrically on the specimens. Moreover, the acquisition parameters of the acoustic emission system were as follows: the threshold was set to eliminate the background noise at 45 dB, and the acoustic emission waveform was recorded at an acquisition rate of 5 MHz per channel.

The experimental conditions were as follows: reverse torque applied to the $[45°]_6$ shaft (the fibre was subjected to compressive load, and the interface was subjected to tensile load). The forward torque load was applied to the $[45°]_{10}$ shaft (the fibre was subjected to tensile load, and the interface was subjected to compressive load). In the torsional strength experiment, the torque was loaded from 0 Nm, with a step size of 1 Nm, until the specimen fractured; finally, the specimen lost its load-carrying capacity and was deemed to be damaged.

3.2. Experimental Results

The torsional strength experiment results are presented in Table 1. The SiC_f/Ti composite had a compression strength greater than its tensile strength. Thereby, the torsional strength of the $[45°]_6$ shaft was slightly greater than that of the $[45°]_{10}$ shaft. The specimens were damaged, and the fractures of the specimens were cut, as shown in Figure 9.

Table 1. Experimental results of the specimens.

Layer Scheme	Torque (M) Direction	Experiment Value/Nm	Fracture Status
$[45°]_6$	Reverse	−11,812	Cracks in 45° and 90° directions
$[45°]_{10}$	Positive	10,418	Cracks in 90° direction

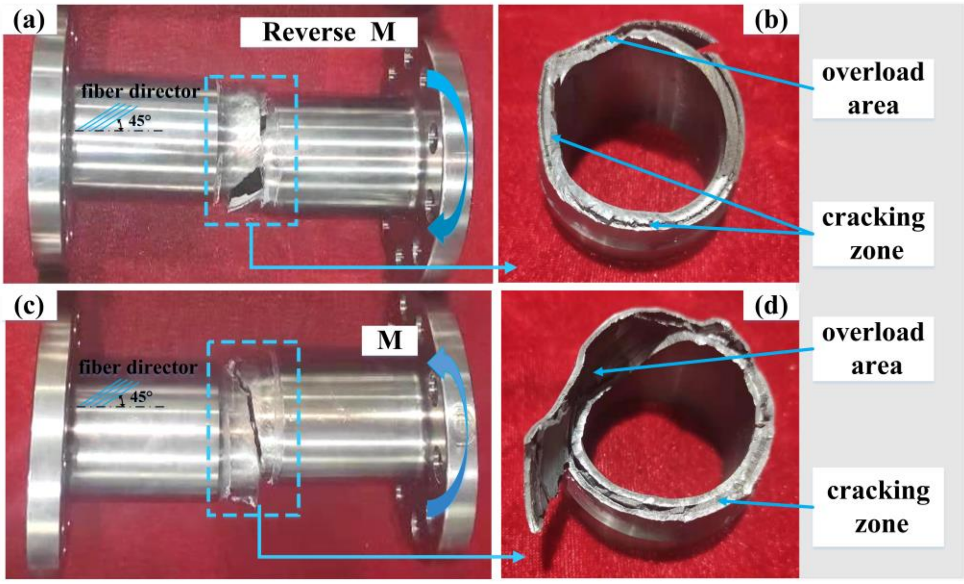

Figure 9. Damage mode and fracture morphology: (**a**) $[45°]_6$ shaft damage mode; (**b**) $[45°]_6$ shaft fracture morphology; (**c**) $[45°]_{10}$ shaft damage mode; and (**d**) $[45°]_{10}$ shaft fracture morphology.

3.2.1. $[45°]_6$ Shaft Failure Mode Analysis

In acoustic emission monitoring of Ti metal matrix composites, 40–60 dB is mostly used for interface cracking, 60–80 dB is used for matrix cracking, and over 90 dB is for fibre fracture [30]. When the torsional load gradually increased from 0 Nm, the interface was first damaged under the tensile stress, and the interface damage signal of 40–60 dB was monitored by acoustic emissions, as shown in Figure 10a. As shown in Figure 11a,b, the interface exhibits obvious debonding. It is shown that, after interface debonding, a flat and regular 45° crack is formed along the fibre direction. After the crack is generated by the SiC fibre-reinforced part, it rapidly expands to the inner and outer titanium matrix of the shaft in the direction shown by the arrow in Figure 11a, which leads to cracking and causes matrix damage. Then, a relatively large number of matrix damage acoustic emission signals—concurrent with interfacial cracking signals—are produced, and the 60–80 dB acoustic emission signal is shown in Figure 10a.

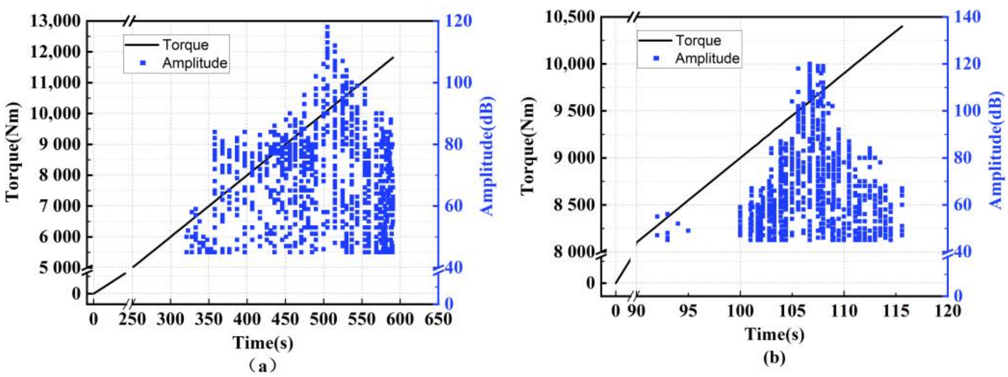

Figure 10. Acoustic emission monitoring experiment results: (**a**) $[45°]_6$ shaft results; (**b**) $[45°]_{10}$ shaft results.

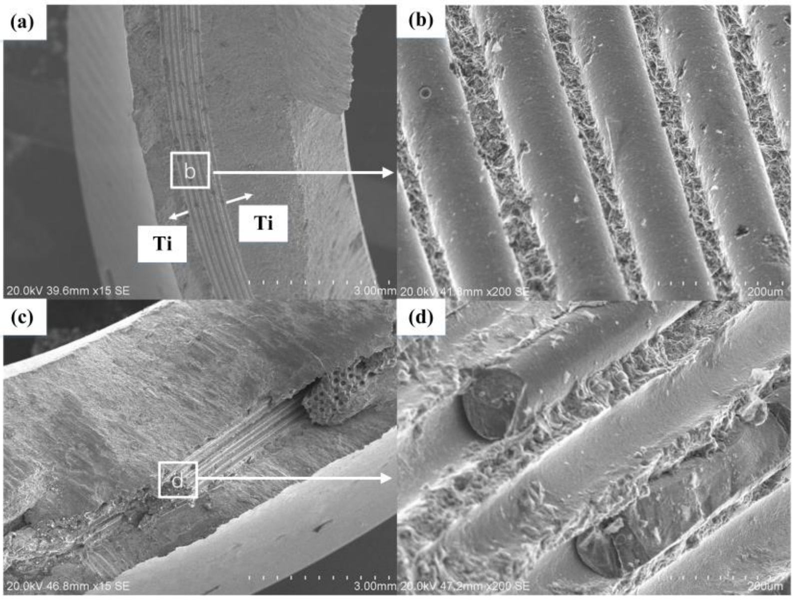

Figure 11. Electron microscope image of $[45°]_6$ fracture: (**a**) 45°fracture crack opening direction; (**b**) 45° fracture interface debonding; (**c**) 90° fracture fibre shearing; and (**d**) 90° fracture fibre damage.

The 90° region observation results are illustrated in Figure 11c,d; a large amount of shear plastic deformation of the titanium matrix occurred along the 90° direction under shear stress. A large number of fibres were also sheared on the fracture, and fibre splitting, C coating dehiscence, and local delamination could occur. W wire cleaning, SiC deposition, and C coating deposition were realized in the same reaction vessel during the preparation of the SiC product. The C coating was between the SiC fibre and matrix, which ensured that the fibre and sputtered matrix have close bonding and no gaps. This improves the performance of the material. Under reverse-torque loading, the fibre was compressed, and the SiC fibre and C coating were separated under compression loading. C coatings were brittle and broke in multiple places under compression loading, resulting in C coating dehiscence and local delamination. In addition, many fibre fracture signals > 90 dB finally appear in Figure 10a, which clearly indicates that the SiC fibres were sheared in large quantities, driven by the titanium matrix.

3.2.2. $[45°]_{10}$ Shaft Failure Mode Analysis

Shafts with this number of plies exhibit a small amount of interface damage signal at first, followed by a matrix damage signal, concentrated at 60–80 dB, and, subsequently, by a large amount of fibre damage acoustic emission signal higher than 90 dB, as shown in Figure 10b. The SiC fibres were sheared in large quantities, driven by the matrix, followed by a large number of 40–60 dB interfacial damage signals. When the fibres were fractured, the interface exhibited delamination damage.

Figure 12a,b show that the fibre fracture was mainly in the titanium matrix in the 90° direction, while the SiC fibres did not fracture strictly in one plane when they were carried off by the titanium matrix. Therefore, the SiC fibre fracture surface had some undulations. Further, during the twisting process of the shaft, the titanium matrix on both sides of the fracture extruded and rubbed each other, leading to the formation of a large area of plastic deformation. More shear tough nests appeared in the titanium matrix on the shaft fracture, which is a typical ductile fracture feature. From the abovementioned observations, it can be concluded that, during torsional static loading, a large amount of plastic deformation of the titanium matrix occurs under the action of shear stress. The titanium matrix drives the SiC fibres to shear fracture, which eventually leads to overall damage to the specimen.

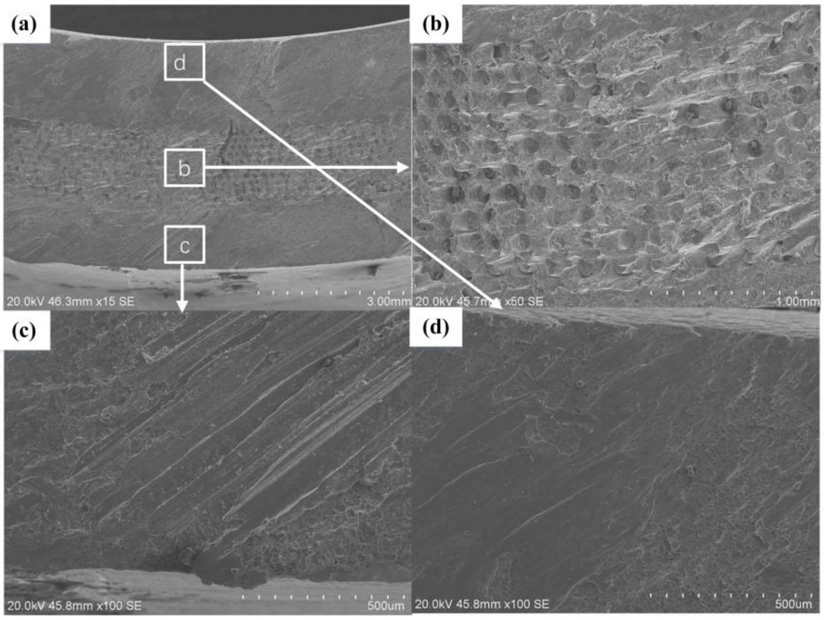

Figure 12. View of $[45°]_{10}$ fracture electron micrograph: (**a**) cross-sectional view of 90° fracture; (**b**) neat fibre cut; (**c**) outer clad titanium plastic deformation zone; and (**d**) inner clad titanium plastic deformation zone.

4. Numerical Simulation Analysis Methods and Models

4.1. Definition of Plane Stress

A schematic of a hollow homogeneous shaft subjected to torque is shown in Figure 13. The orientation of an element of the material, which is aligned with the axial/circumferential direction, is also shown in Figure 13, along with the shear stress [15,16] τ associated with this element orientation. The stress state associated with a general element orientation θ is included in Figure 13, along with those of the $\theta = 0°$ and $\theta = 45°$ orientations. It should be noted that θ defines the plane on which the stress acts, such that the planes defined by $\theta = 0°$ and $\theta = 90°$ carry purely shear stresses, while the planes defined by $\theta = \pm 45°$ carry purely direct stresses. The fibres were wound onto the shaft at 45°. The 45° fibre orientation caused the fibre direction to be perpendicular to the $\theta = 45°$ plane, as defined in Figure 13. This is the plane of the maximum tensile stress.

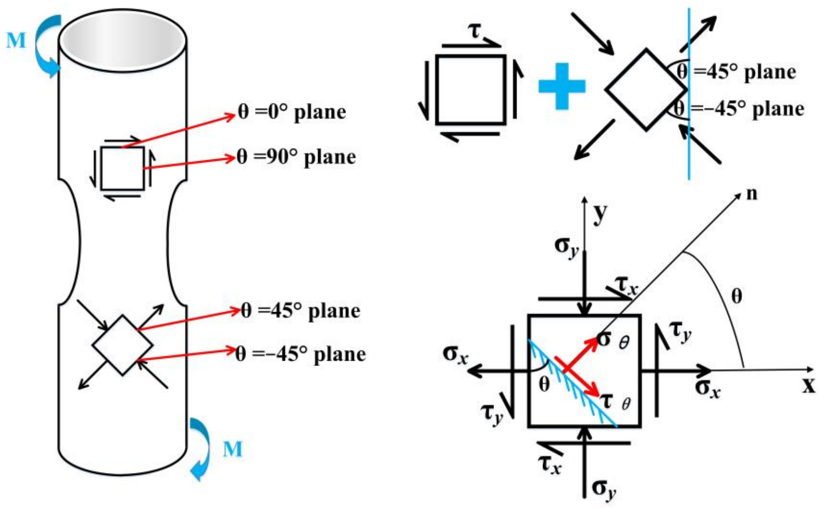

Figure 13. Macro–micro mechanical stress transformation.

4.2. Numerical Calculation Model

Based on the cross-scale mechanical theoretical framework, the macro-mechanical drive shaft models corresponding to Figure 6 were constructed, as shown in Figure 14a. The composite (SiC/TC_4) material parameters, the fibre and matrix (SiC and Ti) material parameters, and the interface parameters (TiC) are presented in Table 2. For the SiC/TC_4 composite shaft, the critical failure loads of fibres and the matrix were predicted by applying progressive torque to the finite element model based entirely on the experimental load conditions.

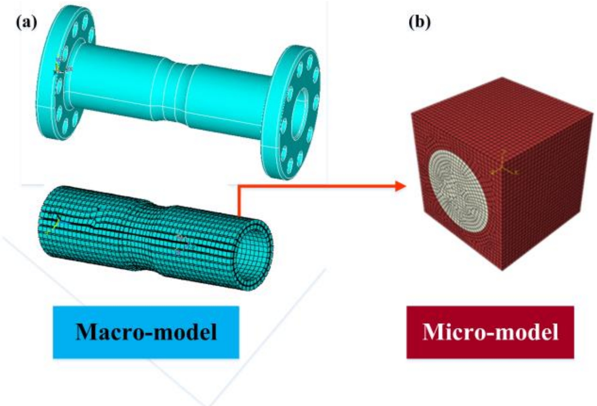

Figure 14. Numerical calculation model: (**a**) the shaft model and (**b**) the RVE model.

Table 2. Material parameters.

Material	E/GPa		μ		G/GPa		
SiC/TC_4	E_1	234	μ_1	0.23	G_1		64.38
	E_2	187	μ_2	0.27	G_2		71.69
	E_3	187	μ_3	0.23	G_3		64.38
Material	E/GPa		μ		X_t/MPa	X_c/MPa	S/MPa
SiC	400		0.17		1800	1800	900
Ti	110		0.30		950	1100	510
Material	E/GPa		μ		X_t/MPa	X_c/MPa	δ_n^{fail}/mm
TiC	330		0.3		98.5	98.5	0.0005

Based on the 3D Hashin failure criterion, the user-defined field (USDFLD) damage subroutine is prepared to simulate the damage of each component during the test. In the calculation process, the load is increased step by step, the stress state at the integral of each element is calculated, and the damage index is calculated according to the stress state of the element, which is stored in the state variable SDV. Therefore, we define SDV to be the maximum damage index (MDI). If MDI is 0, no damage occurs temporarily. The greater the MDI, the greater the degree of damage. When the MDI increases to 1, the element fails, resulting in stiffness degradation. Stress analysis is continued until the entire structure fails.

The damage subroutine of the micro RVE model was employed to simulate the damage of the interface that occurs during the experiment [34]. Through macro-mechanical calculations, for the shaft, the actual stress of the dangerous position element was extracted, and the actual stress was applied to the RVE model after the macro-mechanics transformation. After loading, the response result of the interface could be obtained. The presence of damage was judged according to the stress state of the element, and MDI was calculated; when MDI reached the value of 1, the element at the integration failed, and stiffness degradation occurred. The stress analysis of the fibres and the matrix continued until the failure of the entire shaft [35].

The RVE model was established using a fibre diameter of 100 μm and a fibre volume fraction of 35%. Moreover, the quadrilateral representative volume element model, with a side length of 150 μm, was established according to $L = R\sqrt{\pi/V_f}$, as shown in Figure 14b;

the C3D8R cell was selected for the fibre and matrix. The cohesive element (COH3D8) based on the bilinear cohesion model was also selected for the interface, periodic boundary conditions were applied, and meshing was performed.

5. Results and Discussion

The results of the model torsional strength calculation are shown in Figure 15. In particular, the $[45°]_6$ model exhibited different degrees of reduction in the stiffness at points a, b, c, d, e, and f as the load increased, and final fracture occurred at 10,281.7 Nm. The $[45°]_{10}$ model exhibited failure primarily at the interface, matrix, and fibre between 9000 Nm and 10,000 Nm, and finally fractured at 9545 Nm.

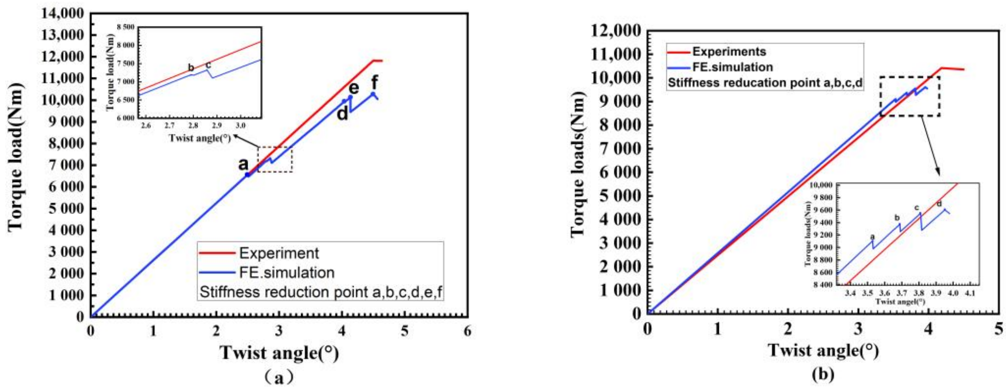

Figure 15. Comparative analysis of the torsional strength calculation results and experiments: (**a**) $[45°]_6$ model; (**b**) $[45°]_{10}$ model.

5.1. $[45°]_6$ Model Calculation Results and Validation

5.1.1. Interface Damage

Based on the macro–micro mechanics transformation method in Section 4.1, the stress of the danger position element of the model (the danger element appeared in layer 6) was extracted by calculating the response results of the $[45°]_6$ shaft model under torque, which were transformed into transverse and longitudinal loads, and then added realistically to the RVE model. The MDI of the interface of the RVE model was also calculated, and the corresponding value under different loads was obtained, as shown in Figure 16. The applied torque started from 0 Nm; when the torque reached −6552 Nm, the interface exhibited cracking and the MDI reached 1, as shown in Figure 16d. This torque is the interface critical cracking load, which corresponds to point a in Figure 15a, which reflects the appearance of interface cracking. Then, stiffness fracture occurred, which is consistent with the interface cracking signal monitored by acoustic emissions, as shown in Figure 10a. The MDI of the matrix and fibre had not reached 1 for all layers before the interface cracked. The damage process of the matrix and fibre can be observed using a macroscopic model with increasing load.

5.1.2. Matrix Damage

When damage occurs at the interface, cracks are generated. The cracks extend into the titanium matrix, resulting in matrix damage, which corresponds to points b and c in Figure 15a under tensile stress. This result is also consistent with the acoustic emission experimental results in Figure 10a.

Figure 17 shows that, when the torque reached −7194.46 Nm, matrix damage failure appeared from layer 6 and extended to layer 4, and the MDI of layer 6 was 1.014. This result shows that, when the torque reached −7322.29 Nm, all layers of the reinforced section started to exhibit different degrees of matrix damage. Additionally, the matrix damage trend extended from the failure initiation position to the ends of the model in Figures 17 and 18. The trend of the matrix damage was extended from the failure initiation position to both ends of the model, and the damage zone was gradually increased from layer 1 to layer 6, with a 45° damage trend in the reinforced section of layers 1, 2, and 3. When the torque load reached −10,136.80 Nm, as shown in Figure 19, the 6th-layer matrix was almost completely damaged. The matrix damage zone almost covered the U-shaped reinforced section of the model, and the damage zone was perpendicular to the axial direction, exhibiting a 90° damage trend. This result is consistent with the angle of the electron microscope experiment results in Figure 9b.

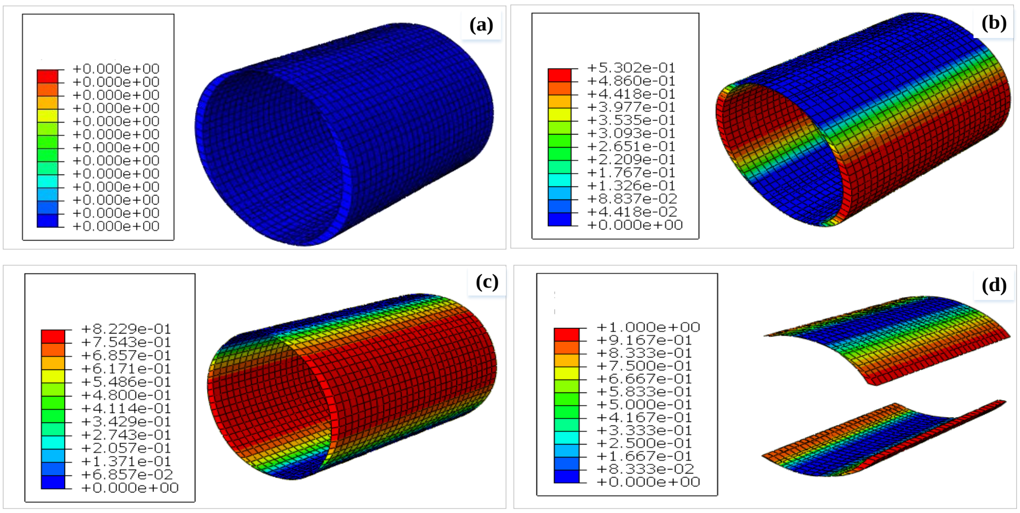

Figure 16. MDI of the interface element of the $[45°]_6$ RVE model: (**a**) M = −2000 Nm; (**b**) M = −4000 Nm; (**c**) M = −6000 Nm; (**d**) M = −6552 Nm.

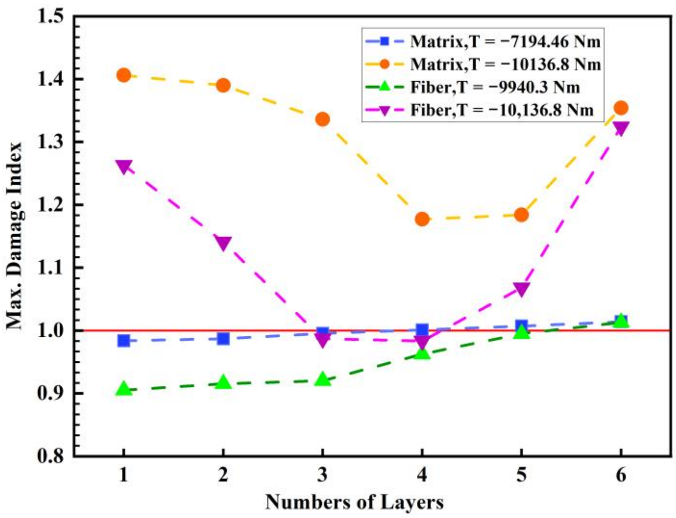

Figure 17. MDI of a matrix of the $[45°]_6$ model under different loads.

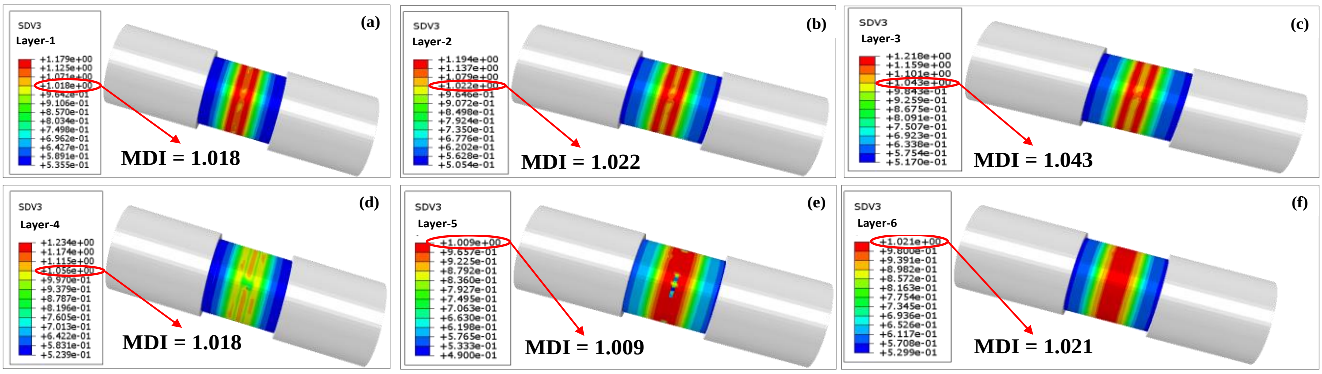

Figure 18. M = −7322.29 Nm matrix MDI: (**a**–**f**): 1st layer–6th layer.

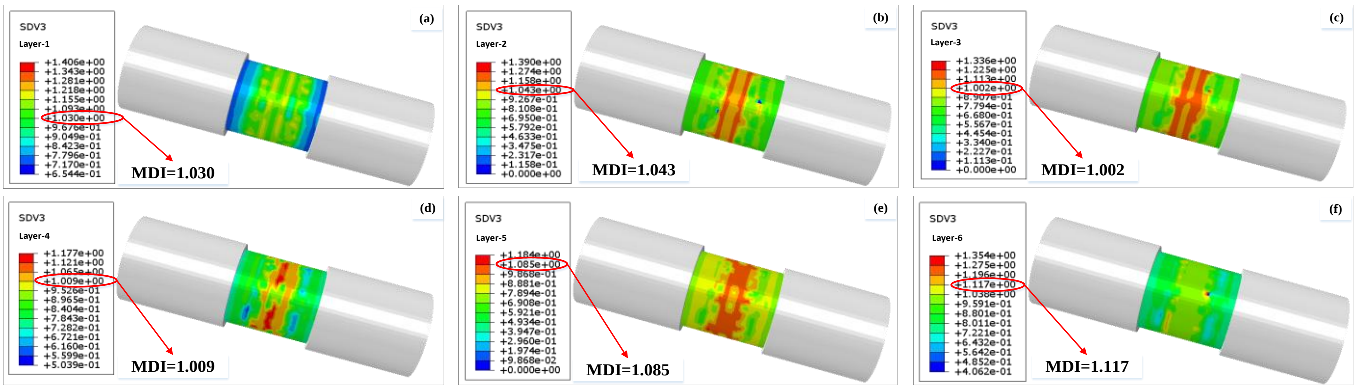

Figure 19. M = −10,136.80 Nm matrix MDI: (**a**–**f**): 1st layer–6th layer.

5.1.3. Fibre Damage

When the torque reached −9940.31 Nm, the MDI of layer 6 fibres reached 1.013, which indicates that the fibres exhibited damage first; this corresponds to the stiffness fracture at point d in Figure 15a. This outcome is consistent with the signal of interface cracking monitored by the acoustic emission shown in Figure 10a. The large amount of plastic deformation that occurred after the damage to the matrix led to the fracture of the SiC fibres. Point e in Figure 15a shows the stiffness reduction corresponding to fibre damage when the load reached −10,136.80 Nm. The trend of MDI values of each layer of the fibre and matrix under this load is shown in Figure 17; the trend of the MDI of the matrix and fibre was the same. When the 1st and 6th layers of the matrix in the reinforced section almost failed, the matrix became useless and debonding with the fibre led to the inability to equalize the load. Therefore, the fibres experienced transverse instability, resulting in the fibre MDI of the 1st and 2nd layers reaching 1, along with the 5th and 6th layers, which began to lose stability and fail. This result means that the model started to crack from the 1st and 6th layers to the intermediate layers of the reinforced section. Point f in Figure 17a shows the stiffness fracture corresponding to the fibre damage when the load reached −10,282.00 Nm, at which time all layers of the fibres in all directions fractured.

The damage zone of the fibres gradually became larger with increases in torque; when the torque reached −10,136.80 Nm, a large number of fibres were sheared short by the titanium matrix, and the fibre failure area was extended in the 45° direction, as shown in Figures 20 and 21, which corresponds to the fibre ply angle. When the torque increased to −10,282.00 Nm, all layers of the fibres failed to fracture. The damaged area almost covered the entire U-shaped section, as illustrated in Figure 22, and the layers gradually lost their load-bearing properties. Finally, catastrophic damage occurred due to the loss of the load-bearing properties.

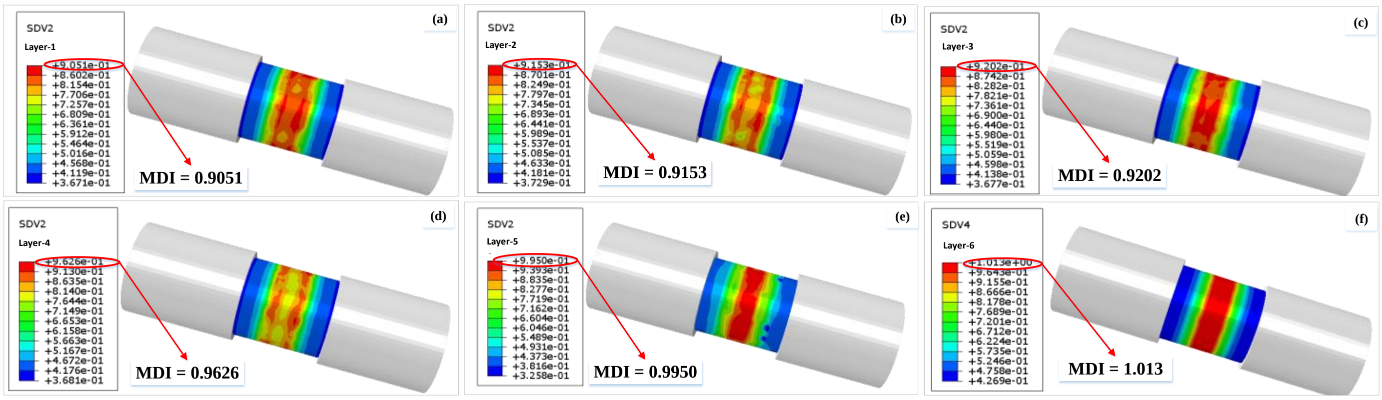

Figure 20. M = −9949.13 Nm fibre MDI: (**a**–**f**): 1st layer–6th layer.

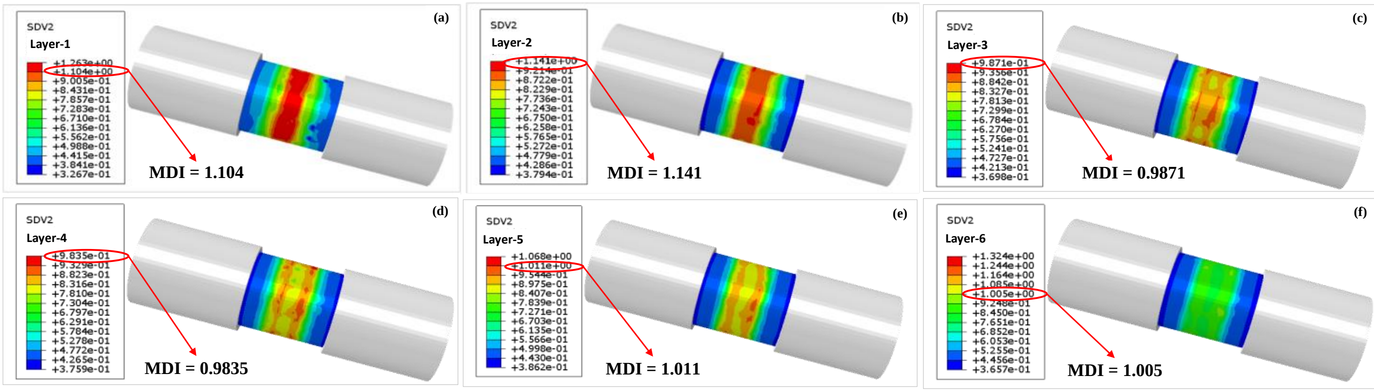

Figure 21. M = −10,136.80 Nm fibre MDI: (**a**–**f**): 1st layer–6th layer.

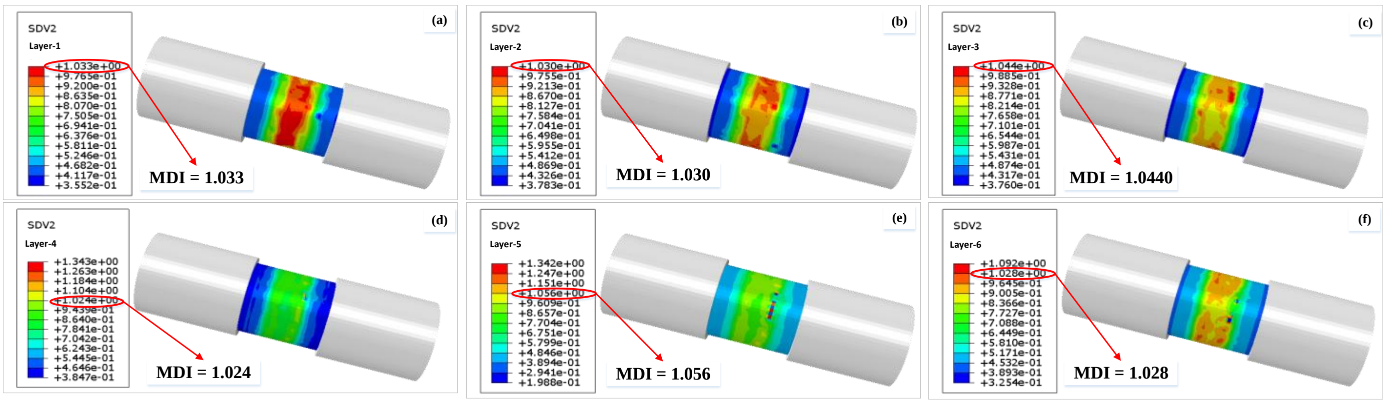

Figure 22. M = −10,282.00 Nm fibre MDI: (**a**–**f**): 1st layer–6th layer.

5.2. [45°]$_{10}$ Model Calculation Results and Validation

5.2.1. Interface Damage

Similar to the [45°]$_6$ model, the MDI calculation results of the interface under different loads are shown in Figure 23. The torque started from 0 Nm, the model was subjected to a positive torque load, and the interface was subjected to pressure. When the torque load reached 9108 Nm, the interface failed and cracks were generated, while the MDI reached the value of 1. This torque is the critical load for interface failure. In the torsional strength calculation, as shown in Figure 15b, point a is the stiffness reduction of the [45°]$_{10}$ model after the appearance of interface cracking. Therefore, the first failure mode to occur in the numerically calculated model was interface failure, which was consistent with the signal of interface cracking monitored by acoustic emissions, as shown in Figure 10b. The MDI of the matrix and fibre did not reach 1 for all layers when the torque load reached 9108 Nm. The damage process of the matrix and fibre for every layer can be observed by the macroscopic model with increasing load.

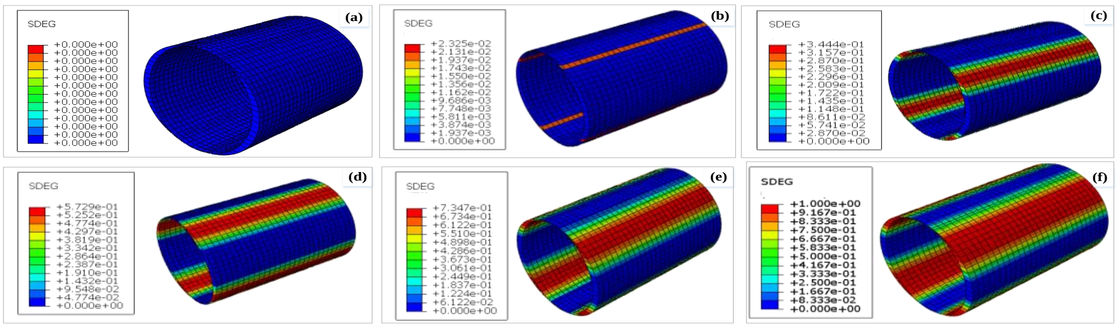

Figure 23. MDI of the interface element of the $[45°]_{10}$ RVE model: (**a**) M = 1000 Nm; (**b**) M = 3000 Nm; (**c**) M = 5000 Nm; (**d**) M = 7000 Nm; (**e**) M = 9100 Nm; and (**f**) M = 9108 Nm.

5.2.2. Matrix Damage

The critical load for interface failure was 9108 Nm, and after crack failure at the interface, it instantly extended transversely to the matrix, and matrix failure occurred immediately afterwards. When the load reached 9396.46 Nm, the matrix in the reinforced section of the model failed, as shown in Figure 24. The MDI of the 10th layer was 1.019, extending inward to the 8th layer, and the failure of the interface and matrix occurred almost simultaneously. Point b in Figure 15b represents the stiffness reduction corresponding to the appearance of matrix damage; this result is basically consistent with the acoustic emission experimental results. As the load increased, when the torque reached 9554.38 Nm, the matrix damage extended inward from the 10th layer to the 1st layer, as shown in Figure 24. The MDI exhibited a decreasing trend from the outer layer to the inner layer; the damaged area also gradually became larger from the 1st layer to the outer layer, and the damaged area of the 10th layer was the largest and the most severe, as shown in Figure 25. Point c in Figure 15b shows the corresponding stiffness reduction after the failure of the matrix of all layers, at which time the matrix no longer had the ability to carry and transfer force. Thereby, more load was transferred to the destabilized fibres, which were then carried by these fibres.

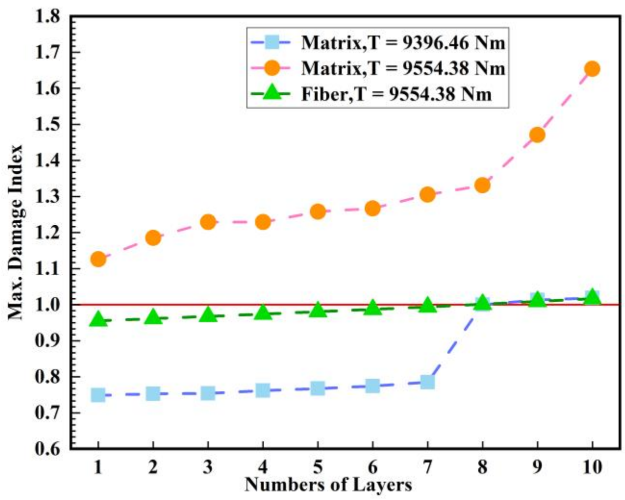

Figure 24. MDI of fibres of the $[45°]_{10}$ model under different loads.

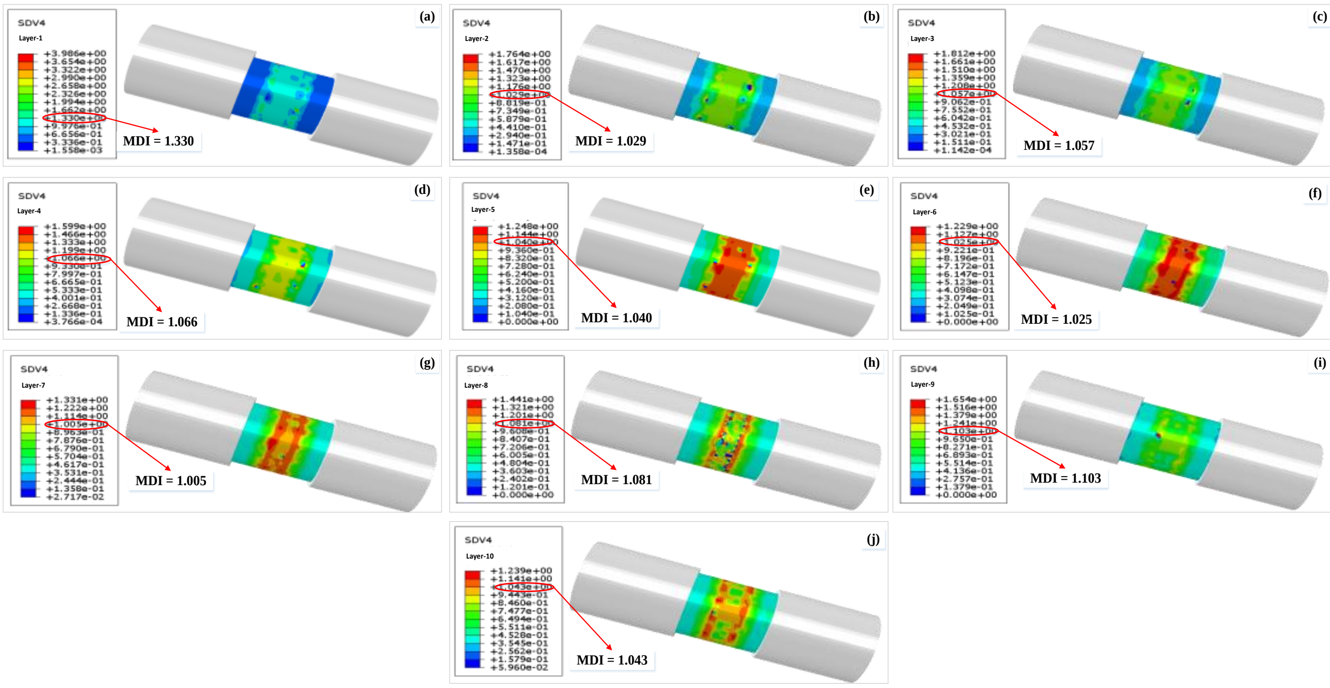

Figure 25. M = 9554.38 Nm matrix MDI: (**a**–**j**):1st layer–10th layer.

5.2.3. Fibre Damage

When the torque load reached 9554.38 Nm, all layers of the matrix had failed to varying degrees since they could not match the original material stiffness, and the structure became laterally destabilized. At this time, the fibres were nearly providing all the load-bearing capacity; then, the fibres began to fail, and the calculated MDI of the fibres is shown in Figure 24. A few fibres broke in the 8th, 9th, and 10th layers; the MDI decreased gradually from the 10th layer to the 8th layer. The load continued to increase, the matrix damage area gradually became larger, and the fibres quickly lost all support. The fibre strength was very high, but the fibres lost the role of the matrix transverse support and dispersion of the force, leading to rapid transverse fracture in the fibres. When the load reached 9601.85 Nm, all layers of the fibres failed, and the reinforced section between the layers of the matrix was rapidly sheared off by the matrix in large quantities. Point d in Figure 15b denotes the stiffness reduction caused by the fibre damage, and the fibre failure zone is at an angle of 90° to the axial axis of the axial structure model, as shown in Figure 26. This result is consistent with the macroscopic fracture electron microscopy test results.

When the SiC_f/TC_4 composite shaft was subjected to forward/reverse torque, damage occurred first at the outermost layer of the reinforced section composite layer, and the damage extended from the outside to the inside. All of this damage started at the interface because of the particularity of the interface strength. SiC fibres and Ti form a thermodynamically non-equilibrium system. During the process of composite formation and high-temperature operation, chemical reactions and element diffusion will inevitably occur between the matrix and fibre, forming a certain thickness of the interfacial reaction layer. The residual stress is mainly concentrated near the interface between the fibre and matrix and along the fibre axial and circumferential direction. The fibre is compressed, and the matrix is under tensile stress. Along the radial direction of the fibre, both the fibre and the matrix are compressively stressed. This is an important factor in determining the strength of the interface. The two damage processes have the same point at which they start from the interface; however, the difference is that, due to the interface being subjected to different loads, slow damage occurs under reverse loading, while fast damage occurs in forward loading.

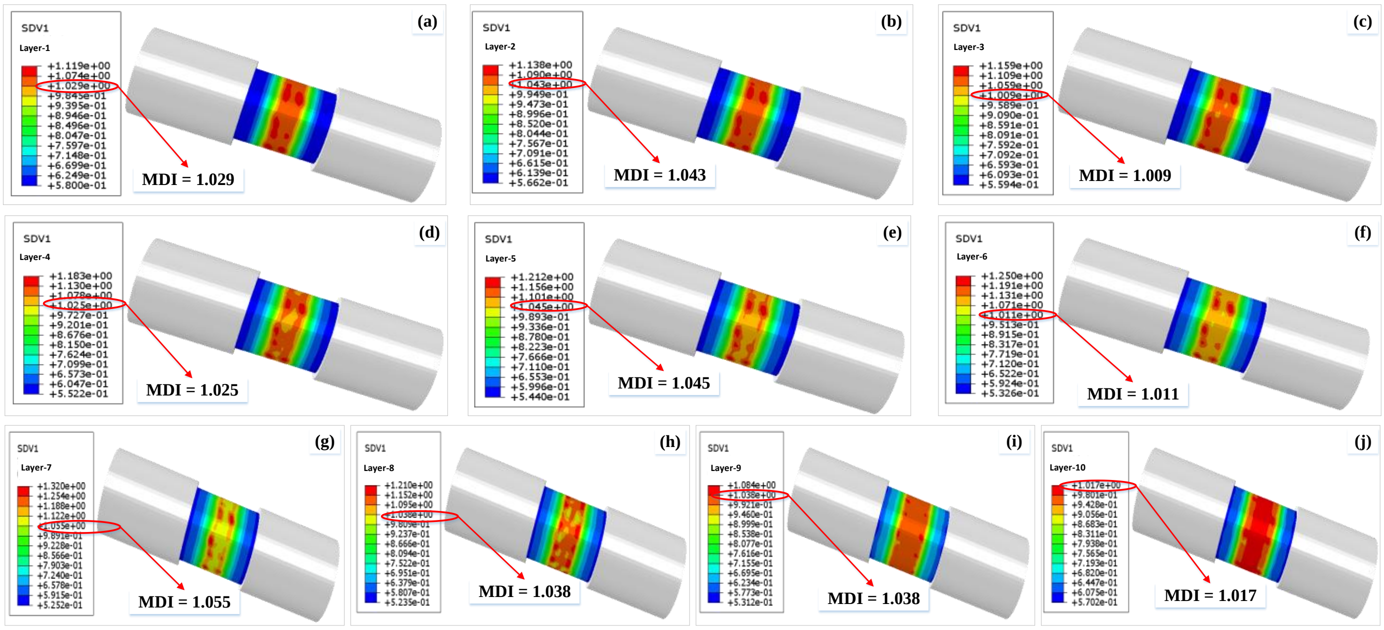

Figure 26. M = 9601.85 Nm matrix MDI: (**a**–**j**):1st layer–10th layer.

6. Conclusions

The progressive damage process and failure mode of the SiC_f/TC_4 composite shaft under forward/reverse torque were thoroughly investigated using cross-scale models, and the following conclusions were obtained.

(1) For the $[45°]_6$ model, when the reverse torque increased, the interface was subjected to tensile load. The interface first cracked at −6552 Nm; it exhibited a large number of cracks after expansion to the matrix, resulting in the matrix stiffness reducing, followed by matrix failure. When the matrix failed, the protection of the fibres was lost; the fibres became destabilized, and, finally, fibre fracture occurred. Therefore, the interface failed under a small torque, and the matrix and fibre then failed sequentially, where interface cracking was the main form of failure. The final failure load was −11,812 Nm, and the entire damage process was a slow change process.

(2) For the $[45°]_{10}$ model, as the forward torque increased, the interface was subjected to compressive load. When the load reached 9108 Nm, the interface failed, instantly extending transversely to the matrix. Followed by the matrix failure, the failure of the interface and matrix occurred almost simultaneously, primarily owing to fibre fracture. The final failure load was 10,418, and the entire damage process was a fast change process.

(3) The composite driving shaft is widely used in aero-engines; under positive torque, the torque magnitude must be relatively small, as operation is frequent. In contrast, under reverse torque, the torque magnitude can be considerably larger, as it is only experienced occasionally.

Author Contributions: Conceptualization, Y.H.; Validation, Y.S.; Formal analysis, J.W.; Data curation, F.Z.; Project administration, L.L. All authors have read and agreed to the published version of the manuscript.

Funding: The authors would like to acknowledge the China Aviation Industry Cooperation Project (No. HFZL2018CXY019) and the Scientific Research Fund of Liaoning Education Department (Grant No. JYT20220534).

Informed Consent Statement: Informed consent was obtained from all subjects involved in the study.

Data Availability Statement: All the data have been reflected in the paper.

Conflicts of Interest: The authors declare no conflict of interest.

References

1. Sha, Y.D.; Ding, G.Y.; Tian, J.G.; Luo, L.; Luan, X.C. Prediction of mechanical properties and experimental verification of fiber reinforced composites. *J. Aerosp. Power* **2018**, *33*, 2324–2332.
2. Gu, C.; Feng, G.; Mi, G. Advances in the Welding of Aluminum Matrix Composites: A New Open Special Issue in Materials. *Materials* **2022**, *15*, 5335. [CrossRef] [PubMed]
3. Talreja, R.; Singh, C.V. *Damage and Failure of Composite Materials*; Zhang, X.J., Li, H.Y., Shu, H.M., Eds.; National Defense Industry Press: Beijing, China, 2021.
4. Chen, G.; Bezold, A.; Broeckmann, C. Influence of the size and boundary conditions on the predicted effective strengths of particulate reinforced metal matrix composites (PRMMCs). *Compos. Struct.* **2018**, *189*, 330–339. [CrossRef]
5. Kim, D.Y.; Choi, H.J. Recent Developments towards Commercialization of Metal Matrix Composites. *Materials* **2020**, *13*, 2828. [CrossRef] [PubMed]
6. Infante, V.; Freitas, M.; Fonte, M. Failure analysis of a crankshaft of a helicopter engine. *Eng. Fail Anal.* **2019**, *100*, 49–59. [CrossRef]
7. Luo, L.; Sha, Y.D.; Hao, Y.P. Method of failure mode analysis and experimental verification for fiber reinforced composites turbo-shaft structure. *J. Aerosp. Power* **2020**, *35*, 1425–1436.
8. Hooker, A.; Doorbar, P.J. Metal Matrix Composites for Aeroengines. *J. Mater. Sci. Technol.-Lond.* **2000**, *16*, 725–731. [CrossRef]
9. Gallicchio, V.; Lodato, V.; De, S.R.; Rengo, S. Fracture Strength and Failure Modes of Endodontically Treated Premolars Restored with Compact and Hollow Composite Posts Subjected to Cyclic Fatigue. *Materials* **2022**, *15*, 1141. [CrossRef]
10. Bartnicki, J.; Tomczak, J.; Pater, Z. Limits of the Process of Rotational Compression of Hollow Stepped Shafts. *Materials* **2019**, *12*, 3049. [CrossRef]
11. Gupta, M. Metal Matrix Composites-The Way Forward. *Appl. Sci.* **2020**, *10*, 3000. [CrossRef]
12. Samuel, D.S.; Howard, F.M.; Bert, J.S. Design and manufacture of a titanium matrix composite low pressure turbine shaft for turbo-shaft engines. *Am. Helicopter Soc. Int. 58th Am. Helicopter Soc. Int. Annu. Forum* **2002**, *58*, 549–553.
13. Spring, S.; Kurz, W.; Krishnamurthy, K.; Peterson, M.; Merrick, H.; Ravenhall, R.; Smith, B. The Development of a Fiber-Reinforced Titanium Matrix Composite Low Pressure Turbine Shaft for Turboshaft Engines. *Am. Helicopter Soc. Int. 59th Am. Helicopter Soc. Int. Annu. Forum* **2003**, *15*, 1622–1626.
14. Trifkovic, D.; Slobodan, N.S.; Srdjan, B.; Milos, M.; Branimir, K.; Zoran, R.; Momir, D. Failure analysis of the combat jet aircraft rudder shaft. *Eng. Fail Anal.* **2011**, *18*, 1998–2007. [CrossRef]
15. Thoms, H.H.; Kraisorn, P.; Adib, A.B. Elasto-plastic finite element analysis of titanium metal matrix composite shafts under torsional loading. *J. Strain Anal. Eng.* **2014**, *50*, 199–216.
16. Thomas, H.H.; Kraisorn, P.; Becker, A. Experimental failure investigation for a titanium metal matrix composite with +45° and ±45° fibre orientation. *J. Mater. Sci. Des. Appl.* **2015**, *229*, 51–63.
17. Ostaszewska-Liżewska, A.; Nowicki, M.; Szewczyk, R.; Malinen, M.A. FEM-Based Optimization Method for Driving Frequency of Contactless Magnetoelastic Torque Sensors in Steel Shafts. *Materials* **2021**, *14*, 4996. [CrossRef]
18. Hou, N.; Ding, N.; Qu, S.; Guo, W.M.; Liu, L.; Xu, N. Failure modes, mechanisms and causes of shafts in mechanical equipment. *Eng. Fail Anal.* **2022**, *136*, 106216. [CrossRef]
19. Gu, J.; Li, K.; Su, L. A Continuum Damage Model for Intralaminar Progressive Failure Analysis of CFRP Laminates Based on the Modified Puck's Theory. *Materials* **2019**, *12*, 3292. [CrossRef]
20. Waqas, H.M.; Shi, D.; Tong, L.; Imran, M.; Qureshi, S.R. Conceptual Design of Composite Bridge Sandwich Structure. *Appl. Sci.* **2020**, *11*, 214. [CrossRef]
21. Gao, G.; An, L.; Giannopoulos, I.K.; Han, N.; Ge, E.; Hu, G. Progressive Damage Numerical Modelling and Simulation of Aircraft Composite Bolted Joints Bearing Response. *Materials* **2020**, *13*, 5606. [CrossRef]
22. Riccio, A.; Costanzo, C.D.; Gennaro, P.D.; Sellitto, A.; Raimondo, A. Intra-laminar progressive failure analysis of composite laminates with a large notch damage. *J. Eng. Fail Anal.* **2017**, *73*, 97–112. [CrossRef]
23. Zhang, C.; Li, N.; Wang, W.Z.; Wieslaw, K.B.; Fang, H.B. Progressive damage simulation of triaxially braided composite using a 3D meso-scale finite element model. *Compos. Struct.* **2015**, *125*, 104–116. [CrossRef]
24. Himayat, U.; Khurshid, A.; Muhammad, I.; Afzal, H.; Vadim, V.S. Simulation of buckling-driven progressive damage in composite wind turbine blade under extreme wind loads. *J. Eng. Fail Anal.* **2022**, *140*, 106574.
25. Han, Z.; Wang, K.; Lu, L.; Wu, Y.S. Fatigue damage assessment method of turbine shafts' torsional vibrations under SSO incidents. *J. Eng. Fail Anal.* **2019**, *105*, 627–637. [CrossRef]
26. Jeng, S.M.; Yang, J.M.; Yang, C.J. Fracture mechanisms of fiber-reinforced titanium alloy matrix composites Part III: Toughening behavior. *Mater. Sci. Eng. A* **1991**, *138*, 181–190. [CrossRef]
27. Yang, Q.; Xie, W.H.; Meng, S.H.; Du, S.Y.; Li, Y.X. Multi-scale analysis method of composite and damage simulation of typical component under tensile load. *J. Acta Mater. Compos. Sin.* **2015**, *32*, 617–624.
28. Ren, X.; Li, J. Multi-scale based fracture and damage analysis of steel fiber reinforced concrete. *J. Eng. Fail Anal.* **2013**, *35*, 253–261. [CrossRef]
29. Echaabi, J.; Trochu, F.; Gauvin, R. Review of failure criteria of fibrous composite materials. *Polym. Compos.* **1996**, *17*, 786–798. [CrossRef]
30. Divse, V.; Marla, D.; Joshi, S.S. 3D progressive damage modeling of fiber reinforced plastics laminates including drilling-induced damage. *Compos. Part A-Appl. Sci. Manuf.* **2022**, *163*, 107230. [CrossRef]

31. Liu, Y.S.; Chen, X.H.; Wu, Z.Y.; Shi, L.; Li, J.P. Effect of axial yarn distribution on the progressive damage behavior of braided composite tube subjected to three-point bending. *Thin Wall Struct.* **2022**, *181*, 110123. [CrossRef]
32. Weibull, W.J. A Statistical Distribution Function of Wide Applicability. *Appl. Mech.* **1951**, *18*, 293. [CrossRef]
33. Xu, K.; Wang, Y.M.; Xu, Z.; Yang, Q.; Zhang, G.X.; Yang, L.N.; Yang, R. Monitoring damage evolution in a titanium matrix composite shaft under torsion loading using acoustic emission. *Acta Metall. Sin.-Engl.* **2019**, *32*, 1244–1252.
34. Sun, Q.P.; Asqardoust, S.; Sarmah, A.; Jain, M. Elastoplastic analysis of AA7075-O aluminum sheet by hybrid micro-scale representative volume element modeling with really-distributed particles and in-situ SEM experimental testing. *J. Mater. Sci. Technol.* **2022**, *123*, 201–221. [CrossRef]
35. Tan, S.C. A progressive failure model for composite laminates containing openings. *J. Compos. Mater.* **2016**, *25*, 556–577. [CrossRef]